

Baryon impact on weak lensing peaks and power spectrum: low-bias statistics and self-calibration in future surveys

Xiuyuan Yang^{1,4,5}, Jan M. Kratochvil², Kevin Huffenberger², Zoltán Haiman^{3,5}, Morgan May⁴

¹ *Department of Physics, Columbia University, New York, NY 10027, USA*

² *Department of Physics, University of Miami, Coral Gables, FL 33124, USA*

³ *Department of Astronomy and Astrophysics, Columbia University, New York, NY 10027, USA*

⁴ *Physics Department, Brookhaven National Laboratory, Upton, NY 11973, USA and*

⁵ *Institute for Strings, Cosmology, and Astroparticle Physics (ISCAP),
Columbia University, New York, NY 10027, USA*

Peaks in two-dimensional weak lensing (WL) maps contain significant cosmological information, complementary to the WL power spectrum. This has recently been demonstrated using N-body simulations which neglect baryonic effects. Here we employ ray-tracing N-body simulations in which we manually steepen the density profile of each dark matter halo, mimicking the cooling and concentration of baryons into dark matter potential wells. We find, in agreement with previous works, that this causes a significant increase in the amplitude of the WL power spectrum on small scales (spherical harmonic index $\ell \gtrsim 1,000$). We then study the impact of the halo concentration increase on the peak counts, and find the following. (i) Low peaks (with convergence $0.02 \lesssim \kappa_{\text{peak}} \lesssim 0.08$), remain nearly unaffected. These peaks are created by a constellation of several halos with low masses ($\sim 10^{12} - 10^{13} M_{\odot}$) and large angular offsets from the peak center ($\gtrsim 0.5 R_{\text{vir}}$); as a result, they are insensitive to the central halo density profiles. These peaks contain most of the cosmological information, and thus provide an unusually sensitive and unbiased probe. (ii) The number of high peaks (with convergence $\kappa_{\text{peak}} \gtrsim 0.08$) is increased. However, when the baryon effects are neglected in cosmological parameter estimation, then the high peaks lead to a modest bias, comparable to that from the power spectrum on relatively large-scales ($\ell < 2000$), and much smaller than the bias from the power spectrum on smaller scales ($\ell > 2,000$). (iii) In the 3D parameter space (σ_8, Ω_m, w), the biases from the high peaks and the power spectra are in different directions. This suggests the possibility of “self-calibration”: the combination of peak counts and power spectrum can simultaneously constrain baryonic physics and cosmological parameters.

PACS numbers: PACS codes: 98.80.-k, 95.36.+x, 98.65.Cw, 95.80.+p

I. INTRODUCTION

Weak gravitational lensing (WL) by large-scale cosmic structures has emerged as one of the most promising methods to constrain the parameters of both dark energy (DE) and dark matter (DM) (e.g. ref. [1]; see also recent reviews in refs. [2, 3]). WL was first detected over two decades ago [4]. It has recently matured to deliver cosmological constraints; in particular, the COSMOS survey has provided independent evidence of the accelerated expansion of the Universe [5, 6]. Over the next decade, revolutionary large WL datasets are expected to be available. The LSST survey will cover 20,000 square degrees with multi-band imaging suitable for weak lensing, and other large surveys will cover several thousand square degrees [7]. These WL datasets will be a rich source of cosmological information, going beyond traditional two-point statistics such as the power spectrum.

Lensing peaks, defined as local maxima in two-dimensional WL maps, provide statistics that will be automatically available and particularly straightforward to measure in lensing datasets. Since they probe the underlying 3D density fluctuations on small, non-linear scales, they are sensitive to non-Gaussian features. As a cosmological probe, the peak counts are therefore complementary to the WL power spectrum, and are similar to

galaxy cluster counts. A major advantage of peaks and a motivation for their use is that they avoid the issue of having to identify genuine bound clusters and measure their masses. Accurate modeling of peak statistics requires large numerical simulations, which are now becoming feasible.

In the past few years, interest in lensing peaks and other, closely related statistics has increased significantly.¹ The probability distribution function of the convergence [9], and its cumulative version, the fractional area of “hot spots” on convergence maps [10] are similar to peak counts in the high-convergence limit and have been shown to have useful cosmology sensitivity. The latter statistic is also known as V_0 , one of the three Minkowski functionals (MFs) for two dimensional thresholded fields. MFs are related to peaks and had been proposed as a weak lensing statistic [11, 12]. More recently, ref. [13] constructed an analytical approximation to V_2 , the genus statistic (which also corresponds to peak counts in the high-threshold limit). The full set of Minkowski

¹ To our knowledge, lensing peaks were first considered as a cosmology probe in the early ray-tracing simulations by ref. [8], which studied the Ω_m -dependence of the peak counts.

functionals in the context of weak lensing was studied extensively both theoretically [14] and in ray-tracing simulations [15]. Finally, peak counts have also been studied in wavelet space [16], and found to break the usual (σ_8, Ω_m) -degeneracy that exists between models from the power spectrum alone.

Preliminary studies [17, 18] that defined peaks as local maxima were based on 2D projections of the 3D mass distribution in low-resolution simulations. WL peak counts with ray-tracing were subsequently studied by refs. [19, 20] and more recently in ref. [21]. These were based on simulations with better mass resolution, and revealed that low-amplitude peaks (which typically do not correspond to single collapsed dark matter halos) contain most of the cosmological information. Various other aspects of WL peak counts have been further explored. Peaks have been shown [22, 23] to constrain the primordial non-Gaussianity parameter f_{NL} . Ref. [24] investigated the origin of the cosmologically important low peaks, and found that they are typically caused by a constellation of 4–8 low-mass halos. Ref. [15] and [25] demonstrated that cosmological constraints from peaks can be tightened by combining several angular smoothing scales. WL peak counts have also been directly compared and found superior to two other commonly used non-Gaussian statistics, skewness and kurtosis [26]. Finally, [27] study the effect of masked regions on shear peak counts and show that using Karhunen-Loève analysis can mitigate biases on peak count distributions caused by masks, and that it can reduce the number of noise peaks.

A common limitation to all of the above works is that they are based on cold dark matter (CDM) simulations (where simulations have been used), neglecting baryons and all astrophysical processes. This leaves an incomplete description of the potential fluctuations and the corresponding lensing signatures. This is a particular concern since previous work has shown that the cooling and condensation of baryons inside dark matter halos can change the total matter distribution and has a large impact on the WL power spectrum on small scales (e.g. refs. [28–30]). Furthermore, in astrophysical models that include feedback from active galactic nuclei (AGN) and supernovae, in addition to cooling and star formation, the matter distribution can be affected well outside dark matter halos, modifying the 3D matter power spectrum [31], as well as the 2D WL power spectrum [32] out to large scales.

Motivated by these findings, here we quantify the effect of baryons on the statistics of WL peaks. Realistic modeling of the astrophysics, using hydrodynamical simulations, remains challenging, both in terms of including all of the relevant physical processes correctly, and also in terms of computational scale. However, previous studies have shown that the cooling and condensation of baryons, and the resulting impact on the total (gas+DM) density profiles of halos, can be modeled by simple modifications to the halo density profile [28–30, 32, 33]. In particular,

ref. [33] finds that a simple increase in the concentration parameter of the universal NFW [34] profile can be a good approximation to the results of hydrodynamical simulations, and can account for the changes in the WL power spectrum [30]. We therefore follow this prescription, and manually steepen the density profile of each individual DM halo identified in our N-body simulations.

This method is simple to use, and allows us to quantify the effects of gas cooling. A similar approach could be followed to model the effect of AGN feedback and other processes, but we leave this to future work. In this paper, we make a large change to the concentration (increasing it by 50%, compared to the 36% increase that was found to match simulation results [30]), thus intentionally amplifying the impact of baryon cooling on the weak lensing statistics.

The main goal of this paper is to investigate the bias in the cosmological parameters w , σ_8 and Ω_m when peak counts and power spectra are fit neglecting baryonic effects. Our results suggest that the bias from the peaks is lower, and also in a different direction, compared to the power spectrum. This suggests that the power spectrum and peak counts can be combined to “self-calibrate” WL surveys, i.e. to fit cosmological parameters simultaneously with parameters describing the halo profiles.

The rest of this paper is organized as follows. In § II, we describe our calculational procedures, including the creation of the WL maps through ray-tracing in N-body simulations, identifying halos and modifying their density profiles, and creating “baryonic” versions of WL maps. This section also presents our statistical methodology to compare maps, and our Monte Carlo procedure of estimating confidence contours and the biases caused by neglecting the baryonic effects. In § III, we present our results, which include the effect of baryon cooling on the peak counts and on the power spectrum, as well as the biases caused by neglecting these effects when fitting for the three cosmological parameters w , σ_8 and Ω_m . In § IV, we offer a detailed discussion of our main results, as well as of several caveats and possible extensions. Finally, in § V, we summarize our main conclusions and the implications of this work.

II. METHODOLOGY

A. N-body simulations and WL maps

The cosmological N-body simulations of large-scale structures and ray-traced weak lensing maps used in this paper are the same as those in our earlier work [15, 24]. We refer the reader to these publications for a full description of our methodology; here we review the main features and describe the new features we have implemented to model the baryonic effects. We intend to make our data products publicly available in the future [35, 36].

A total of 80 CDM-only N-body runs were made with the INSPECTOR GADGET lensing simulation pipeline

[35, 36] at the New York Blue supercomputer. NY Blue is part of the New York Center for Computational Sciences at Brookhaven National Laboratory/Stony Brook University.

Our suite of 7 cosmological models includes a fiducial model with parameters $\{\Omega_m = 0.26, \Omega_\Lambda = 0.74, w = -1.0, n_s = 0.96, \sigma_8 = 0.798, H_0 = 0.72\}$, as well as six other models. In each of these six models, we varied one parameter at a time, keeping all other parameters fixed at their fiducial values; we thus have WL maps in variants of our fiducial cosmology with $w = \{-0.8, -1.2\}$, $\sigma_8 = \{0.75, 0.85\}$, and $\Omega_m = \{0.23, 0.29\}$. Note that in the last case, we set $\Omega_\Lambda = \{0.77, 0.71\}$ to keep the universe spatially flat.

To produce the N-body simulations, we first created linear matter power spectra for the seven different cosmological models with CAMB [37] for $z = 0$, and scaled them back to the starting redshift of our N-body simulations at $z = 100$ following the linear growth factor. Using these power spectra to create initial particle positions, the N-body simulations were run with a modified version of the public N-body code GADGET-2 [38] and its accompanying initial conditions generator N-GENIC. We modified both codes to allow the dark energy equation of state parameter to differ from its Λ CDM value ($w \neq 1$), as well as to compute WL-related quantities, such as comoving distances to the observer, at each simulation cube output. Each simulation contains 512^3 CDM particles in a cubic box with a side length of $240h^{-1}$ comoving Mpc, allowing a mass resolution of $7.4 \times 10^9 h^{-1} M_\odot$. Each of these runs took approximately 1.75 real clock days, using 64 processors on the Blue Gene.

In each of the six non-fiducial cosmological models, we ran 5 strictly independent N-body simulations (i.e. each with a different realization of the initial conditions). To minimize the differences between two cosmologies arising from different random realizations, the initial conditions for each of those five simulations were matched across the cosmologies quasi-identically. This entails recycling the same random number when drawing mass density modes from the power spectrum for each cosmology (note that the power spectra themselves of course differ across the cosmologies). In the fiducial cosmology, we ran 50 strictly independent simulations – the first set of 5 to match the other cosmologies quasi-identically as mentioned above, and an additional set of 45 to improve the statistical accuracy of the predictions in the fiducial cosmology (especially the covariance matrices). For the “baryonic” maps, as described below, only the first of these 50 simulations was used. Table I lists the sets of simulations in our suite, along with their cosmological parameters, the number of independent N-body runs, and the number of pseudo-independent 12 deg^2 maps (see below).

To create the raw WL convergence maps, we used a standard two-dimensional, flat-sky ray-tracing algorithm closely following [39] with minor modifications as described in detail in [20]. Earlier work with similar algorithms includes [40–42]. Cubes with particle posi-

WL map set	σ_8	w	Ω_m	Ω_Λ	# of N-body sims	# of WL maps
45-sim fiducial	0.798	-1.0	0.26	0.74	45	1000
5-sim fiducial	0.798	-1.0	0.26	0.74	5	1000
$\Omega_m = 0.23$	0.798	-1.0	0.23	0.77	5	1000
$\Omega_m = 0.29$	0.798	-1.0	0.29	0.71	5	1000
$w = -1.2$	0.798	-1.2	0.26	0.74	5	1000
$w = -0.8$	0.798	-0.8	0.26	0.74	5	1000
$\sigma_8 = 0.75$	0.750	-1.0	0.26	0.74	5	1000
$\sigma_8 = 0.85$	0.850	-1.0	0.26	0.74	5	1000
NFW-replaced	0.798	-1.0	0.26	0.74	1	200
“baryonic”	0.798	-1.0	0.26	0.74	1	200

TABLE I: *Our weak lensing map sets, including the cosmological parameters, the number of underlying independent N-body simulations, and the number of weak lensing maps in each set.*

tions from the N-body simulations were output every $80h^{-1}$ Mpc in the radial (redshift) direction. While several independent simulations were used to make each map, boxes from the same simulations had to be recycled multiple times. The data cubes at each redshift were therefore randomly shifted, sliced, and rotated (by multiples of 90 degrees) to produce pseudo-independent realizations. The particles were projected onto two-dimensional density planes perpendicular to the central line of sight of the map. The triangular shaped cloud (TSC) scheme [43] was used to place the particles on a grid on these 2D density planes. The Poisson equation was then solved in Fourier space to convert the surface density into a gravitational potential. The deflection angles and convergences were calculated at each plane for each light ray from the first and second transverse spatial derivative of the 2D gravitational potential, respectively. Between density planes, the light rays were assumed to travel in straight lines; 2048×2048 light rays were followed in this fashion for each convergence map. A total of 1,000 pseudo-independent, 12 deg^2 convergence maps were produced in each CDM-only cosmological model; 200 maps were produced in the sets used to study the systematic effect of baryons (see below). The number of maps in each map set is given in the last column of Table I.

To create the final simulated WL maps, for simplicity, we assumed that the source galaxies are confined to the single redshift $z_s = 2$. Ellipticity noise from the random orientations of the source galaxies was added to the convergence maps pixel by pixel, drawing from a Gaussian distribution corresponding a conservative source galaxy surface density of $n_{gal} = 15 \text{ galaxies/arcmin}^2$, and an r.m.s. noise in one component of the shear of $\sigma_\gamma = 0.22$. Once noise was added, we smoothed the maps with a finite version of a $\theta_G = 1 \text{ arcmin}$ 2D Gaussian filter. This corresponds to the single most informative and smallest angular scale on which we trust our maps, based on comparisons with the power spectrum from theoretical predictions (see [15] for details). Combining several smoothing scales would tighten the overall constraints and could change the biases. We expect that this would not change

the qualitative results in this paper, but we leave an investigation of this issue to future work.

Peaks are defined as local maxima on the pixelized final mock WL maps, and are counted in a straightforward fashion, with the convergence in the central pixel κ_{peak} identified as the “height” of each peak. Power spectra are measured numerically from the Fourier transforms of the same maps following standard techniques.

The differences between cosmological models, and thus the cosmological parameter dependence of the peak counts and the power spectra, are computed using pairs of the CDM-only 5-simulation map sets. Additionally, the covariance matrices of both observables – peak counts binned by their height, and power spectrum in bins of ℓ – were computed from the 45-simulation fiducial map set; we have found that this was necessary for better accuracy (see [15] for details). Note that we do not consider the dependence of the covariance matrices themselves on cosmology (in principle, this dependence could help improve constraints).

Finally, in order to study the impact of baryons, we create two more sets of WL maps. These are based on the fiducial CDM model, and a single N-body simulation. In this simulation, we identify all the DM halos in the 3D simulation cubes, and replace them with spherically symmetric halos with analytic NFW [34] density profiles. The ray-tracing procedure is then repeated exactly as before, and a new set of 200 “NFW-replaced” maps is created. This set is used to predict the expectation values of the peak counts and the power spectra in the fiducial cosmology, in the absence of baryons. Finally, beginning with the same 3D data, the concentration parameter “ c ” of each spherical NFW halo is increased by 50%, and the ray-tracing and map-making procedure is once again repeated, to create a corresponding set of 200 “baryonic” maps. This last set is used to find the expectation values of the peak counts and the power spectra in the fiducial cosmology, in the presence of baryon cooling. This procedure guarantees that any differences between an individual “NFW-replaced” map and the corresponding “baryonic” map is caused only by the changes in the halo concentration (and not from the halo replacements or from having different random realizations). Note that ideally we would want 1,000 pseudo-independent realizations of the baryonic maps, to match the number we have for the CDM-only map sets. However, to keep computational costs feasible, we have produced only 200 baryonic maps from a single N-body run. Nevertheless, we replicate each of these 200 baryonic maps 5 times, each time adding a different random noise realization. This provides a better statistical sampling of the noise (in particular, a more accurate determination of the average effect of the noise).

B. Identifying and replacing dark matter halos

In this section we describe in detail how we identify, remove, and re-insert halos into the N-body simulations.

Once the N-body simulations are generated, we use the publicly available AMIGA halo finder ([44], hereafter AHF) to identify collapsed halos in our N-body runs. Its output consists of the 3D positions and the tagged set of particles belonging to each halo, the central position of the halo (defined as the local maxima of the density field), as well as the total number of halo particles inside spherical shells at several different discrete radii, from which the spherically-averaged density profiles can be calculated. Depending on the redshift, AHF identifies a total of $2.5 \times 10^5 - 2.6 \times 10^5$ halos in our box, with masses in the range $1.5 \times 10^{11} h^{-1} M_{\odot} - 5 \times 10^{14} h^{-1} M_{\odot}$. We then remove all the particles belonging to all of the halos from the N-body simulations, and add back the density profiles fitted to the identified halos, assuming halos are spherically symmetric and described by NFW profiles. The details of the fitting will be given in §II C below.

In the procedure of replacing halos, three non-trivial points regarding mass conservation need to be clarified. The first point concerns sub-halos. When a parent halo and a sub-halo share a common structure, the halo finder saves the shared particles in both the parent and the sub-halo profiles. As a result, in our procedure, the particles within halos are removed one time, but the shared parts of halos are added back repeatedly. We have found that this can cause an artificial 5% increase in total (halo plus subhalo) mass. To avoid this problem, and to conserve mass, we sort the halo catalog by mass. Beginning with the lowest-mass halo, we consider halos in this ranked list one-by-one, always comparing the position of the center of a halo with the positions of all of the halos further down the list (with higher masses). If the center of a halo is found to fall inside the virial radius of any of the higher-mass halos, we subtract the mass of the smaller halo from that of the larger one. When we re-insert the larger halo into the 3D simulation box, we use the analytical NFW profile with the reduced mass.

The second point concerns discretization of the analytic NFW profiles. In our map-making procedure, the projected halo density profiles are evaluated only at the discrete grid points on our 2D density plane. As a result, each halo effectively contributes a total mass given by a “2D trapezoidal integral”, rather than its actual (analytically calculable) mass. In principle, the actual halo profiles are known, and the projected mass could be resolved to arbitrary accuracy; in practice, we have found this to be computationally too expensive. Instead, in order to conserve the total mass, we normalize the discretized surface density profile by multiplying by the ratio of the actual mass of the halo and the total projected mass of the discretized profile.

Finally, a third point concerns halos that are “truncated”, either in the transverse direction (because they

are too close to the edge of the 12 deg² map) or in the redshift direction (because they are too close to the back or front side of the underlying 3D simulation slice; note that the raw 3D simulation cubes have periodic boundary conditions, but the slices used to make the maps do not [15]). In the former case, we add the projected halo density profiles as we do for the normal halos, applying periodic boundary conditions. In the latter case, the surface density of a truncated halo is taken by summing the discretized density profile over the region inside the simulation box. We do not re-normalize the profiles of these truncated halos in the redshift direction, because it is difficult to determine how much mass was actually lost in the truncation. However, we have shown in our previous study [24] that the effect of edge halos can be safely ignored for studying the peak counts.

After accounting for the sub-halos and normalizing the discretized profiles, the fractional difference between the total mass removed and the total mass added back is less than 0.2%.

To check the ultimate accuracy of the halo replacement procedure, in Figure 1, we plot the fractional difference in the peak counts and the power spectrum caused by the halo replacement in the fiducial cosmology. The data points are averaged over 100 realizations. For this check, we used the noiseless versions of the WL maps. As the upper panel shows, the halo replacement works very accurately for peaks below $\kappa \lesssim 0.06$. The difference is still smaller than 10% for peaks below $\kappa \lesssim 0.1$, however there is a systematic decrease in the number of peaks that becomes significant for higher amplitude peaks. This decrease is caused by our treatment of the sub-halos. High peaks are typically caused by a single massive halo. Massive halos contain many sub-halos, and because of the substantial mass loss due to tidal stripping, sub-halos are found preferentially away from the center of the host halos [45]. Recall that when we add back an NFW parent halo, in order to conserve mass, we subtract the total mass in subhalos. When we perform this subtraction, we assume, for simplicity, that the mass in the subhalos is distributed radially in a smooth fashion, following the density profile of the parent halo. This procedure therefore over-subtracts mass near the halo center, and under-subtracts mass near the halo outskirts. The overall effect of our procedure is to decrease the central density (by a few percent). Since the line of sight to a high peak typically passes very close to the center of the corresponding massive halo, this diminishes the height of the peak, and results in fewer high peaks. A similar explanation holds in the case of the power spectrum, shown in the lower panel. The halo replacement works very accurately for large scales, with $\Delta P/P \lesssim 2\%$ for $l < 1000$. But at $l \gtrsim 5,000$, where the one-halo term dominates the power spectrum, there is a significant ($\sim 6\%$) decrease in power.

We emphasize that the inaccuracies due to halo replacement are quantified here only as a reassurance that we did not, in the process, gravely modify the WL observables. We are only interested in the impact of baryons;

indeed, the impact of baryon cooling in the real 3D halos should be similar to the increase in concentration parameters for the spherically symmetric halos.

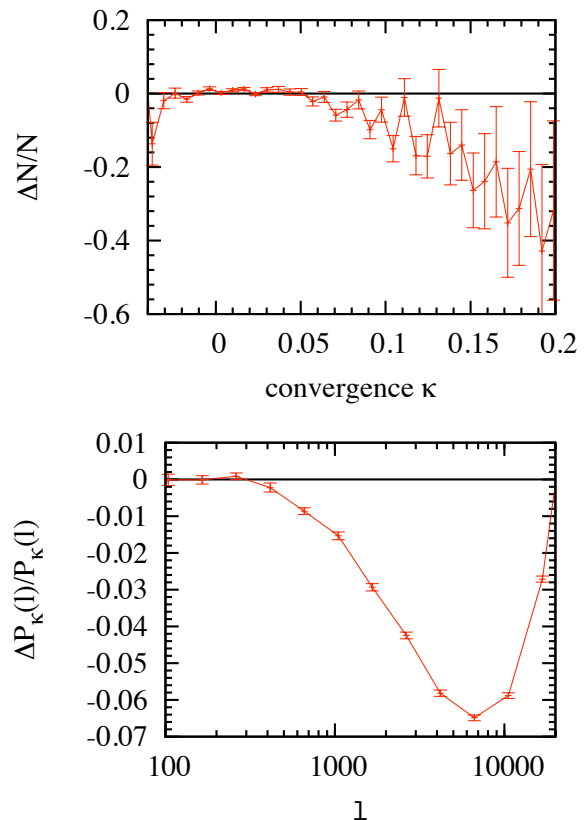


FIG. 1: The effect of replacing halos in our N -body simulations by spherically symmetric NFW halos. In the upper panel, we show the fractional difference $\langle \Delta N \rangle / \langle N \rangle$ in the peak counts caused by this halo replacement, in convergence bins of width $\Delta \kappa = 0.00675$. In the lower panel, we show the corresponding fractional difference in the power spectrum $\langle \Delta P_\kappa \rangle / \langle P_\kappa \rangle$, in logarithmic bins of the spherical harmonic index with a width $\Delta \log \ell = 0.2$. Data points are averaged over 100 realizations. The error bars in the top panel are estimated as the standard deviation of ΔN , divided by $\langle N \rangle$ (and similarly as the standard deviation of ΔP_κ , divided by $\langle P_\kappa \rangle$, for the power spectrum). The source galaxies are assumed to be at redshift $z_s = 2$, and the convergence maps have been smoothed with a 1 arcmin Gaussian filter.

C. Fitting halo density profiles

In this section, we describe our procedure for the fitting the halo density profiles and quantify how well this procedure works.

We assume all halos and subhalos follow a universal NFW profile [34],

$$\rho_{\text{nfw}}(r) = \frac{\rho_s}{(r/r_s)[1 + (r/r_s)]^2} \quad (1)$$

where r is the radius from the halo center, and r_s and ρ_s are a characteristic radius and density. The profile is truncated at R_{180} , inside which the mean overdensity is 180 times the matter density of the universe at redshift z . This convention is consistent with the settings in the AHF halo finder. The concentration parameter is given by $c_{180} \equiv R_{180}/r_s$.

The NFW density profile is uniquely defined by the concentration parameter c_{180} , and the normalization factor ρ_s . To obtain c_{180} , we chose to fit the normalized cumulative density profile $F(x)$, i.e. the fraction of mass within a certain radius r , as a function of $x = r/R_{180}$,

$$F(x) = \frac{\log(c_{180}x + 1) - c_{180}x/(1 + c_{180}x)}{\log(c_{180} + 1) - c_{180}/(1 + c_{180})}. \quad (2)$$

Here R_{180} is taken as the actual radius of halos found by the halo finder. We fit $F(x)$ to find c_{180} and calculate the normalization factor ρ_s as:

$$\rho_s = \frac{M_{180}}{4\pi r_s^3 (\log(c_{180} + 1) - c_{180}/(1 + c_{180}))}. \quad (3)$$

Here M_{180} is the actual halo mass returned by the halo finder. For some halos, we find that c_{180} does not converge to an acceptable number ($1.1 \leq c_{180} \leq 50$), or the halo mass is too low and the halo finder cannot compute a radial profile. We distinguish these as unfitted halos, and for these halos we use an analytical formula to obtain c_{180} , adapted from Eq. (5) in ref. [46]:

$$c_{200} = 4.67 (M_{200}/10^{14}h^{-1}M_{\odot})^{-0.11}/(1+z). \quad (4)$$

Eq. (4) adopts a different convention from ours – the profile is truncated at the radius inside which the mean overdensity is 200 times the critical density of the universe. We therefore extend the NFW profile for a halo with mass M_{200} outward to a radius where the mean interior density is 180 times the background matter density. This extrapolation yields a relation between the input M_{180} and M_{200} that depends on c_{180} ; using Eq. (4) and the definitions of the various quantities above, the parameter $c_{180} = R_{180}/r_s$ can be found iteratively.

The unfitted halos account for $\sim 2\%$ of all halos in our simulations. This is unsurprising, since, for example, halos that are undergoing major mergers, or have not yet relaxed from a recent major merger, have no reason to follow NFW profiles [46].

We find that the rest of our halos follow the NFW profiles accurately. In Figure 2, we show the spherically averaged density profile $\rho(r)r^3$, for a halo with a mass of $8.7 \times 10^{13}h^{-1}M_{\odot}$ at redshift $z = 0$, along with the corresponding best-fit NFW profile. The quality of the fit shown in this figure is typical of halos in our simulations.

As a quantitative test of the accuracy of our fitting, we define a statistic

$$T = \frac{1}{n} \sum_{i=1}^n \left| \frac{F_i - F(x_i)}{F_i} \right|. \quad (5)$$

Here n is the number of data points (i.e. in radius) for one halo, F_i and $F(x_i)$ is the i th data point and the fitted value at that radius. We plot the distribution of T in Figure 3. The figure demonstrates that typically, the NFW profiles are accurate to within 5%, although there is a tail of outliers extending to poorer fits. As mentioned above, approximately 2% of our simulated halos could not be fit by NFW profiles at all (and are not shown in this figure).

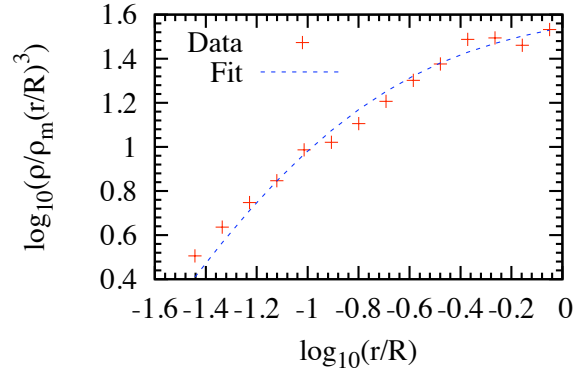


FIG. 2: The figure shows the spherically averaged density profile $\rho(r)r^3$ (red crosses), for a halo with a mass of $8.7 \times 10^{13}h^{-1}M_{\odot}$ at redshift $z = 0$, along with the corresponding best-fit NFW profile (dashed blue curve). The quality of the fit shown in this figure is typical of halos in our simulations. Here ρ_m is the mean matter density of the universe and R_{180} is (approximately) the virial radius of the halo. The best-fit NFW profile was obtained by a least-squares fit to the normalized cumulative density profile (Eq. (2)).

D. Statistics ²

We refer to the different statistics one can obtain from a 2D WL map—e.g. power spectrum, peak counts, etc.—as N_i . The index i in the components N_i of the vector \mathbf{N} labels different heights for the peaks, and different multipoles for the power spectrum. We divide the peak counts into 30 bins in height κ_{peak} in the range $0.023 \leq \kappa_{\text{peak}} \leq 0.08$ and, we use a second set of 30 bins above $\kappa_{\text{peak}} \geq 0.08$. Similarly, we divide the power spectrum into 30 multipole bins ℓ in the range $100 \leq \ell \leq 2 \times 10^4$. For computational reasons, the power spectrum is first pre-computed and stored for 1,000 “pre-bins” spaced linearly in multipole $100 \leq \ell \leq 1 \times 10^5$ and is only later combined into the 30 larger bins used for the final computation.

² This discussion closely follows ref. [15].

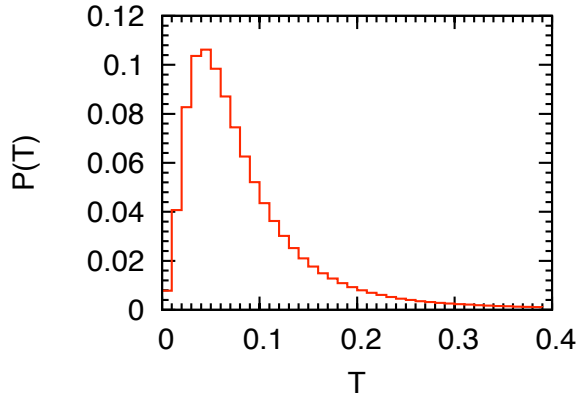


FIG. 3: The distribution of the statistic T , defined as the fractional deviation between the fitted and the actual normalized cumulative density profile (Eq. (5)), averaged over radii, for the halos in our N -body simulations. The figure demonstrates that typically, the NFW profiles are accurate to within 5%, although there is a tail of outliers extending to poorer fits. Approximately 2% of our simulated halos could not be fit by NFW profiles at all (and are not shown in this figure).

To constrain cosmology, we are interested in the true ensemble average, over an infinite number of realizations within a single cosmology (hereafter denoted by brackets $\langle \rangle$) as a function of cosmological parameters $\mathbf{p} = \{\Omega_m, w, \sigma_8\}$, as well as the ensemble covariance.³ Since these are not available, we estimate them from a finite number of our simulations. Averaging over the pseudo-independent map realizations within a given cosmology, we can obtain an estimate for the ensemble average by

$$\langle N_i(\mathbf{p}) \rangle \approx \bar{N}_i(\mathbf{p}) \equiv \frac{1}{R} \sum_{r=1}^R N_i(r, \mathbf{p}), \quad (6)$$

where $N_i(r, \mathbf{p})$ is the statistics vector measured in a single map and r runs over our $R = 1,000$ maps. We call this estimate the *simulation mean*. It differs from the true ensemble average both because of the limited number of realizations and also because of the limitations inherent in our simulations, such as limited resolution. In the absence of a fitting formula for the peak counts in the non-Gaussian case (analogous to the power spectrum formula from [47] in the nonlinear regime) the simulation mean serves as our proxy for theoretically predicted peak counts.⁴

³ More generally, one could utilize the full probability distribution of a statistic, not just its average, as well as the cosmology-dependence of all higher-order correlations, not just the covariance; we will not investigate these issues in the present paper.

⁴ The ensemble average for the peak counts can be computed exactly for a Gaussian random field [48]; however, this is a poor approximation to the lensing peaks [24].

We can form this estimate only for the 7 selected cosmologies where we have run simulations (Table I). For cosmologies with other parameter combinations \mathbf{p} , we have to interpolate (and in a few cases extrapolate) between these 7 points in the 3D parameter space. We thus construct a first-order Taylor expansion around our fiducial cosmology:

$$\bar{N}_i(\mathbf{p}) \approx \bar{N}_i(\mathbf{p}^{(0;\text{NFW})}) + \sum_{\alpha} \frac{\bar{N}_i(\mathbf{p}^{(\alpha;\text{CDM})}) - \bar{N}_i(\mathbf{p}^{(0;\text{CDM})})}{p_{\alpha}^{(\alpha)} - p_{\alpha}^{(0)}} \cdot (p_{\alpha} - p_{\alpha}^{(0)}). \quad (7)$$

The index $\alpha = 1, 2, 3$ refers to either Ω_m, w , or σ_8 , and the sum counts through all 3 parameters. The fraction on the right-hand-side of Eq. (7) is a finite difference derivative along the direction of the parameter α , computed using the fiducial cosmology ($\mathbf{p}^{(0)}$) and a cosmology in which the parameter p_{α} was changed from the fiducial case ($\mathbf{p}^{(\alpha)}$). As mentioned above, the 5-simulation CDM map sets with quasi-identical initial conditions were paired and used for the computation of this derivative, but the simulation mean for the NFW-replaced set was used as the expansion point of the Taylor series (the first term on the RHS). We indicate this explicitly in Eq. (7) by the superscripts “CDM” and “NFW”.

If this non-fiducial cosmology is chosen such that $p_{\alpha}^{(\alpha)} - p_{\alpha}^{(0)}$ is positive for all three parameters, we call it a “forward derivative”, if it is negative, we call it a “backward derivative”. We will also refer below to a “2-sided derivative”, which switches automatically between the forward and backward cases as needed for each parameter, corresponding to the octant in the 3D parameter space where the interpolation is performed. For simplicity, we use the backward derivative throughout this paper unless explicitly noted otherwise (and below we highlight some important differences in our results obtained with other derivatives).

Similarly to the simulation mean, we estimate the ensemble covariance matrix from the simulations, $\text{Cov}(N_i, N_j) \approx C_{ij}$, where

$$C_{ij}(\mathbf{p}) \equiv \frac{1}{R-1} \sum_{r=1}^R [N_i(r, \mathbf{p}) - \bar{N}_i(\mathbf{p})][N_j(r, \mathbf{p}) - \bar{N}_j(\mathbf{p})]. \quad (8)$$

This covariance matrix contains contributions both from the sample variance of the signal and from the galaxy shape noise. In the case of the power spectrum, the Gaussian random noise in different ℓ bins should be uncorrelated, and therefore contribute only diagonal terms (in practice, the cross-terms are small but nonzero in our finite set of realizations). However, adding noise to the maps has a nonlinear effect on peak counts, and introduces off-diagonal terms, as well. As mentioned above, in practice, we only evaluate and use the covariance matrix in our fiducial 45-simulation map set.

E. Monte Carlo parameter estimation contours

Each of our WL maps spans a 12 deg^2 field of view, yet we wish to obtain parameter contours for a $20,000 \text{ deg}^2$ full-sky survey, such as LSST. Thus we employ a parametric bootstrapping approach to generate approximations to full-sky maps. In this procedure, we randomly select a map from our set of 1,000 maps, with replacement, $20,000/12 \approx 1,667$ times. The effective solid angle of this larger “composite map” is then $20,000 \text{ deg}^2$, as desired. The map, of course, is not a true composite – we merely compute the observables for each of the 1,667 patches individually, and then add or average over them to get their values for the full-sky map. We create 10,000 such full-sky maps to obtain smooth parameter contours in our Monte Carlo procedure. While this process cannot generate information not present in the 1,000-map set, the bootstrap procedure has a large benefit. Individual 12 deg^2 maps constrain parameters only poorly, and large fluctuations in N_i require parameter extrapolations far outside the range of our simulations. The averaging in the bootstrap procedure suppresses these fluctuations, so the N_i are similar to those from the simulations.

To estimate the cosmological parameter error contours from the set of baryonic maps, we use χ^2 -minimization to find the best-fit cosmological parameter combination for each of the 10,000 bootstrapped full-sky maps. Here χ^2 is defined by

$$\chi^2(r_b, \mathbf{p}) \equiv \sum_{i,j} \Delta N_i(r_b, \mathbf{p}) [\text{Cov}^{-1}(\mathbf{p}^{(0)})]_{ij} \Delta N_j(r_b, \mathbf{p}) \quad (9)$$

where

$$\Delta N_i(r_b, \mathbf{p}) \equiv N_i(r_b, \mathbf{p}^{(0;\text{baryon})}) - \langle N_i(\mathbf{p}) \rangle. \quad (10)$$

Note that r_b here counts the full-sky maps and therefore runs over $r_b = 1, \dots, 10,000$. For each Monte Carlo realization r_b , we minimize χ^2 with respect to \mathbf{p} using a simulated annealing algorithm. This is a popular technique based on Markov Chain Monte Carlo with a decreasing “temperature”, which helps the algorithm to get out of local minima (we had success with this algorithm in our earlier work [15]). We emphasize that the matrix Cov in Eq. (9) can be reasonably arbitrary and does not even have to be the covariance matrix; this makes this method robust with respect to noise in the covariance matrix estimate [15].

The bootstrapping procedure explained above returns 10,000 sets of best-fit parameters for each full-sky realization; the distribution of these best-fit points can be used to draw confidence contours at desired confidence levels (68% in this paper, unless stated otherwise) based on the density of the best-fit points.

We indeed find that the best-fit points lie within the parameter range of our simulations, so that interpolation can be used during the best-fit procedure. The only exception is the high- ℓ power spectrum, which required

a modest extrapolation in the parameter space. In contrast, the scatter of best-fit points from the original small 12 deg^2 maps was so large that a significant fraction of the best-fits lie outside the simulated region, requiring large extrapolations. Bootstrapping also eliminates the need to re-scale the contours to correspond to a full-sky survey.

III. RESULTS

A. Effect of baryons on the statistics

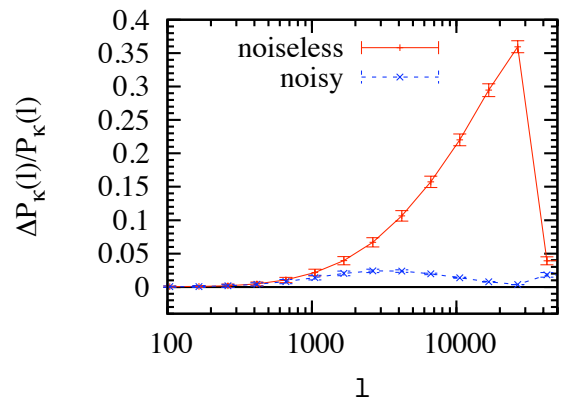


FIG. 4: The fractional difference $\langle \Delta P_\kappa \rangle / \langle P_\kappa \rangle$ in the power spectrum caused by the 50% boost in the concentration parameter of each NFW halo, shown in models without (red solid curve) and with galaxy shape noise (blue dashed curve; the noise corresponds to a source galaxy surface density of $n_{\text{gal}} = 15 \text{ arcmin}^{-2}$ at redshift $z_s = 2$). The data points are averaged over 200 realizations in logarithmic bins of width $\Delta \log \ell = 0.2$. Error bars are estimated as the standard deviation of the ΔP_κ , divided by $\langle P_\kappa \rangle$. We have artificially increased the error bars by a factor of 10 for visual clarity. The smallness of the error bars indicate that the impact of baryons on the power spectrum is highly systematic, i.e. very similar in each realization.

We begin the presentation of our results with the effect of baryons on the statistics themselves. In Figure 4, we show the fractional difference $\langle \Delta P_\kappa \rangle / \langle P_\kappa \rangle$ in the power spectrum, caused by the 50% boost in the concentration parameter of each NFW halo, shown in model with and without galaxy shape noise. The data points are averaged over 200 realizations in logarithmic bins of width $\Delta \log \ell = 0.2$. As the figure shows, in the noiseless case, a 50% increase in concentration causes a strong increase in the small scale power, by about 20% at $\ell = 10^4$. The effect is much smaller on large scales ($\ell \lesssim 2000$). This agrees with the qualitative conclusions in ref. [30], who used a similar toy model. The drop beyond $\ell \gtrsim 3 \times 10^4$ is due to our 1-arcmin smoothing. In the noisy case, the fractional difference has a turnover at the much larger

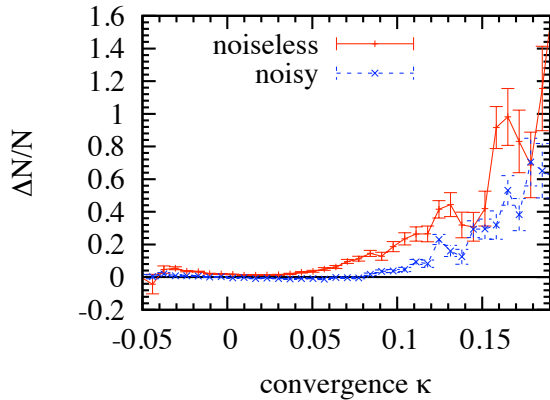


FIG. 5: Similar to Figure 4, except we show the fractional difference in the peak counts, $\langle \Delta N_{\text{peak}} \rangle / \langle N_{\text{peak}} \rangle$, caused by the same 50% boost in the halo concentration parameters. The data points are averaged over 200 realizations, and shown in convergence bins of width $\Delta\kappa = 0.00675$. The error bars are shown at their original size. Compared to the power spectrum, the impact of baryons on the peak counts is less systematic, i.e. varies more significantly between realizations.

scale of $l \approx 3,000$; this is the scale at which the galaxy shape noise starts to dominate. Note that the absolute difference $\langle \Delta P_\kappa \rangle$ in the power spectrum in the noisy case is exactly the same as in the noiseless case. Therefore even the small $< 2\%$ fractional difference in the noisy case can cause a strong bias in inferred cosmology when the baryonic power spectrum is fitted by the non-baryonic model (see detailed discussion below).

In Figure 5, we show the fractional difference in the peak counts, $\langle \Delta N_{\text{peak}} \rangle / \langle N_{\text{peak}} \rangle$, caused by the same artificial 50% boost in the halo concentration parameter. The data points are again averaged over our 200 maps, and shown in convergence bins of width $\Delta\kappa = 0.00675$. As the figure shows, in both the noiseless and the noisy case, there is a strong increase in the number of high peaks, but very little change in the number of low peaks. The reasons why the low peaks are robust to the change in the concentration parameter will be discussed below.

B. Cosmological constraints and biases

We next present the biases in the inferred best-fit cosmological parameters when the baryonic effects are ignored. We define the “low” and “high” peaks to have heights $\sigma_{\text{noise}} \leq \kappa_{\text{peak}} \leq 0.08$ and $\kappa_{\text{peak}} \geq 0.08$, where $\sigma_{\text{noise}} = 0.023$ is the r.m.s. of κ from galaxy shape noise. We similarly define the power spectrum on “very large”, “large”, and “small” angular scales (or “very low”, “low”, and “high” l ranges) to be those with $100 \leq l \leq 1000$, $100 \leq l \leq 2000$ and $2000 \leq l \leq 2 \times 10^4$, respectively. Note that two of these ranges overlap partially.

As described in § II E, we generate the distribution of

best-fit points in the 3-dimensional parameter space of σ_8 , w , and Ω_m . Projecting this 3D distribution in one of the 3 dimensions can then be used to define the 68% joint confidence contours on the remaining two parameters, marginalized over the third. As also described above, the baryonic model was compared to the non-baryonic NFW-replaced model, linearly interpolated with the backward derivative, using noisy maps with $z_s = 2$ and 1 arcmin smoothing. We apply 30 nearly logarithmic bins to the whole range $100 \leq l \leq 2 \times 10^4$ of the power spectrum. Note that this leaves fewer than 30 bins in each of the very low, low and high- l ranges as defined above (namely, 9, 17, and 13 bins, respectively). The nearly logarithmic bins are generated by choosing the bin boundaries so that the 1,000 pre-bins are assigned to 30 bins with nearly equal logarithmic spacing. For very low l , this results in bins that are linearly spaced, because there are not enough pre-bins to achieve truly logarithmic spacing. For the peaks, the bin boundaries are chosen so that each of the 30 bins for the low peaks contains the same number of peaks, and likewise we use 30 equal-count bins for the high peaks. This split in the equal-count procedure avoids having too few bins for the high peaks.

In Figure 6, we show the 68% confidence contours obtained from the peak counts, along with those from the power spectra, for a 2×10^4 -deg² full-sky survey. We have approximately 2,000 low peaks and 250 high peaks in every 12 deg² field. The offsets between the center of the underlying 3D distribution (i.e. the best-fit model in 3D) and the correct fiducial values are listed in Table II, and correspond to the biases on the inferred cosmological parameters. The contours in the 2D plots of Figure 6 are always marginalized over the third parameter that is not displayed, i.e. they are projections of the full 3D best-fit-point distribution onto the 2D plane, and the contours are calculated in this projected space. Recall that we only have 1000 (pseudo-)independent 12 deg² maps, from which 1,666 maps are drawn randomly with replacement in the bootstrapping procedure. As bootstrapping cannot improve the accuracy of the mean, it cannot improve the determination of the locations of the centers of the contours, and affects only their size. The “1 σ ” error of the centroids (in these 2D planes) should therefore be larger than the size of the contours (the 68% confidence levels from the LSST-like survey) by a factor of approximately $\sqrt{1666/1000} \approx 1.3$. This is in the limit that random noise dominates the dispersion in the best-fit locations. In the opposite limit, i.e. if the dispersion is dominated by the variations among the underlying 200 baryonic maps, then the peak likelihood locations in 2D would be larger by an additional factor of $\sqrt{5}$.

From Figure 6, we can roughly estimate that the joint 2D errors from the peak counts extend over $\delta\sigma_8 \approx 0.005$, $\delta w \approx 0.03$ and $\delta\Omega_m \approx 0.005$; the corresponding uncertainties in the locations of the best-fits in 2D are therefore $\delta\sigma'_8 \approx 0.0065$, $\delta w' \approx 0.04$ and $\delta\Omega'_m \approx 0.0065$. A similar estimate can be done for the power spectrum. Given these uncertainties, we conclude that the low peaks

Observable	$\Delta\sigma_8$	Δw	$\Delta\Omega_m$
Low Peaks	0.009	0.01	-0.001
High Peaks	0.061	0.10	-0.024
Low- ℓ Pow. Spec.	0.03	0.11	-0.01
Very Low ℓ Pow. Spec.	0.01	0.07	-0.00
High- ℓ Pow. Spec.	-0.23	-0.58	0.15

TABLE II: *The biases in the three cosmological parameters from the peak counts and power spectrum. The numbers in the table show the offset between the location of the best-fit in 3D and the correct fiducial cosmology along each of the 3 parameters σ_8 , w , and Ω_m .*

and the very low- ℓ power spectrum are both robust to baryonic cooling, with the inferred biases consistent with zero; the exception is that low peaks have a small bias in σ_8 . The high peaks and the high- ℓ power spectrum both have significant biases, $\Delta\sigma_8 \approx 0.061$, $\Delta w \approx 0.10$ and $\Delta\Omega_m \approx -0.024$ from peak counts, and $\Delta\sigma_8 \approx -0.23$, $\Delta w \approx -0.58$ and $\Delta\Omega_m \approx 0.15$ from the power spectrum (see Table II). The low bias, at least within the context of our model, and the high information content of the low peaks suggests the value of including them in cosmological analyses for dark energy (see further discussion in § IV B below).

Perhaps our most interesting result is that the biases from the peaks and the power spectra are in different directions in the 3D parameter space. The bias from the high peaks, in particular, is in a direction nearly opposite from the (much stronger) bias from the high- ℓ power spectrum; they are also in different directions from the low- ℓ power spectrum. This opens up the possibility for self-calibration, whereby baryonic parameters, such as the halo concentration parameter in our case, could be determined simultaneously with the cosmological parameters. Only for the correct concentration parameter will the contours from the different observables align.

C. Bias directions and goodness-of-fit

In this section, we address two important questions related to the above results: (1) what is the quality of the biased best-fits? (2) what determines the direction of the biases? The first question is especially important, since in principle, a poor best-fit can reveal the presence of unaccounted-for parameters.

In Figure 7, we show the peak counts and power spectra in the baryonic model, compared directly to the best-fit baryonless models. The four panels (top left, top right, bottom left, bottom right) show the results for low peaks, high peaks, low ℓ power spectrum and high ℓ power spectrum (following the definitions of the low/high ranges in § III B, and using the corresponding best-fit points in Table II). In each case, the deviations from the baryonless fiducial cosmological model are shown. In each panel, the solid [red] curves show the effect of the baryons, and the dashed [blue] curves show the deviations that best mimic

these curves, achieved in the best-fit baryonless models. As shown by the figure, in all four panels, we find an excellent fit, i.e. the best-fit curves agree well with the baryonic curves. Although the best fit somewhat overpredicts the number of peaks at the high- κ end of the low peaks in the top left panel, we find a total $\chi^2 = 30$. Since we have 30 bins, the fit is good, with a reduced χ^2 of unity (with somewhat better fits in the other three panels). This implies that when the baryonic effects are neglected when fitting the data, the cosmological parameters can be biased, and this will not be obvious from the low quality of the fit.

To investigate the origin of the bias directions, the long-dashed [green], dotted [pink] and dot-dashed [cyan] curves show the effect of changing a single one of the three parameters σ_8 , w , Ω_m at a time, to its best fit value, i.e., the bias in one parameter times the backward derivative of the observable with respect to that. (This means that the green, pink and cyan curves sum up to the blue curve.)

In the case of the low peaks (top left panel), the best fit is driven almost entirely by the bias in σ_8 : the figure shows that the change in σ_8 , by itself, can mimic the baryonic effects quite well.⁵ Furthermore, the small residual would require decreasing the number of peaks at the high- κ end (in bins 20 and higher), while keeping the peak counts in the lower- κ bins unchanged. Such a change in the shape of the peak count distribution can not be accomplished by changing either w or Ω_m ; as a result, these two other parameters remain essentially unbiased.

The case of the high peaks (top right panel) is quite different, with degeneracies between all three parameters playing an important role in the bias. In particular, the changes in the counts due to σ_8 and Ω_m have a strong degeneracy, so that these two parameters work in the opposite direction.⁶ However, the degeneracy is not perfect, and leaves a nonzero residual – interestingly, this residual can be mimicked essentially perfectly by a relatively modest change in w .

Turning to the low- ℓ power spectrum (bottom left panel), the fit is again driven by the bias in σ_8 , but unlike in the case of low peaks, σ_8 alone cannot mimic the baryonic effects. As a result, w and Ω_m play a role, working in the direction opposite to σ_8 , and producing a near-perfect fit.

The most interesting case is the high- ℓ power spectrum, shown in the bottom right panel in Figure 7. Here the degeneracy between σ_8 and Ω_m is so perfect that the changes in these parameters (with opposite sign) essentially cancel each other. As a result, the net change in

⁵ Note that reducing the number of low peaks requires an *increase* in σ_8 ; this somewhat counterintuitive result has been found [20] and explained in detail [24] in our earlier work.

⁶ This $\sigma_8 - \Omega_m$ degeneracy in the abundance of $\sim 3\sigma$ peaks has been noted earlier [19, 24].

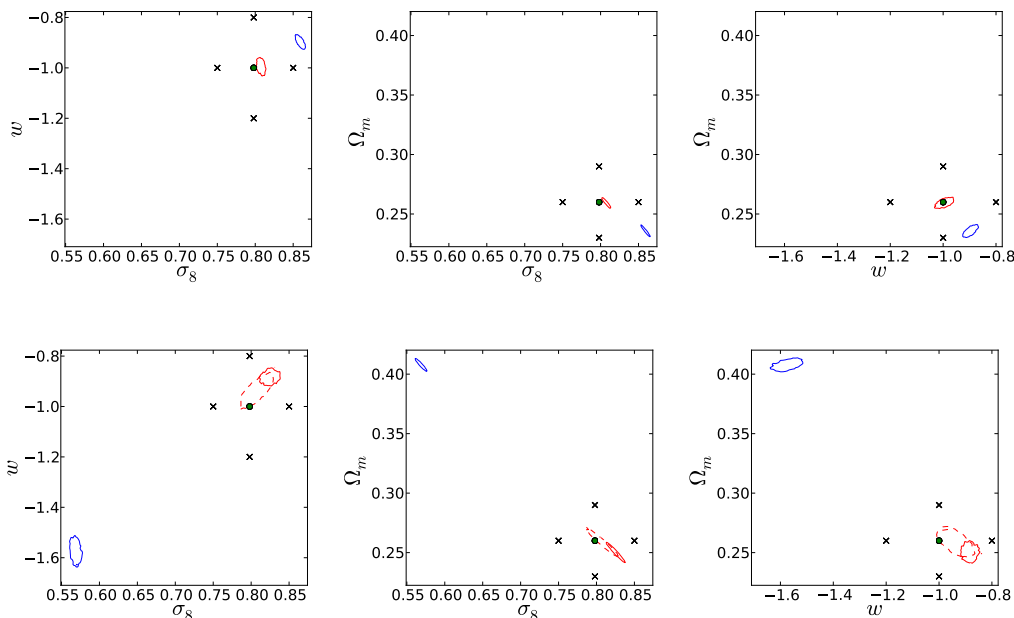


FIG. 6: The joint 68% confidence contours on pairs of cosmological parameters (marginalized over the third), obtained from peak counts and the convergence power spectrum, in a full sky ($2 \times 10^4 \text{deg}^2$) survey. The location of the correct fiducial cosmology is marked by a green dot in each panel. For reference, crosses mark the other cosmologies we simulated. 10,000 Monte-Carlo realizations of the baryonic model were fit by models neglecting the baryon effects, which can produce a bias in the inferred parameters. In the upper panels, results from the low ($\sigma_{\text{noise}} \leq \kappa_{\text{peak}} \leq 0.08$) and high ($\kappa_{\text{peak}} \geq 0.08$) peaks are shown by solid red and solid blue contours. In the lower panels, results from the very-low ($\ell \leq 1000$), low ($\ell \leq 2000$), and high- ℓ ($2,000 \leq \ell \leq 2 \times 10^4$) power spectra are shown by dashed red, solid red and solid blue contours, respectively. The bias is strongest from the small-scale (high- ℓ) power spectrum; it is nearly negligible for the low peaks and for the very-low ℓ power spectrum.

the high- ℓ power spectrum can be attributed almost entirely to the change in w . This explains why there is a very large bias in w . The fact that the bias from the high peaks is driven by σ_8 , whereas the bias from the high- ℓ power spectrum ends up being dominated by w , makes it less surprising that the biases from high peaks and the high ℓ power spectrum are in very different directions.

IV. DISCUSSION

A. Robustness of the inferred bias

How robust are the results to the number of bins? Our results about biases have not been optimized over the number and placement of bins. We have found, in general, that all the results listed in the last section hold qualitatively, as long as the number of bins used is not too small. In Table III, we show the biases of the three cosmological parameters σ_8 , w , Ω_m inferred from the peak counts, with three different numbers of bins, using noisy maps with $z_s = 2$. Bin boundaries were chosen such that each bin contains the same number of peaks. The table shows that the biases from the low peaks are quite stable; as the number of bins is varied from 20 to 30, the

Observable	bins	$\Delta\sigma_8$	Δw	$\Delta\Omega_m$
Low Peaks	20	0.014	0.01	-0.004
	25	0.009	0.03	0.001
	30	0.009	0.01	-0.001
High Peaks	20	0.057	0.16	-0.020
	25	0.069	0.07	-0.030
	30	0.061	0.10	-0.024

TABLE III: The inferred biases of the three cosmological parameters σ_8 , w , Ω_m from the peak counts, using three different number of bins. Low and high peaks are always defined to be those with heights between $\sigma_{\text{noise}} \leq \kappa_{\text{peak}} \leq 0.08$ and $\kappa_{\text{peak}} \geq 0.08$; with $\sigma_{\text{noise}} = 0.023$. Bin boundaries were chosen such that each bin contains the same number of peaks.

changes in the biases are always less than the uncertainty on the bias ($\delta\sigma'_8 \approx 0.0065$, $\delta w' \approx 0.04$ and $\delta\Omega'_m \approx 0.0065$ as mentioned above). High peaks have larger changes in the corresponding biases than the low peaks, but the sizes of these fluctuations are still comparable to the uncertainties. We conclude that our qualitative results from the peak counts are robust as long as $\gtrsim 20$ peak-height bins are used.

How does the result depend on the finite difference derivatives? To compute the inferred biases, the bary-

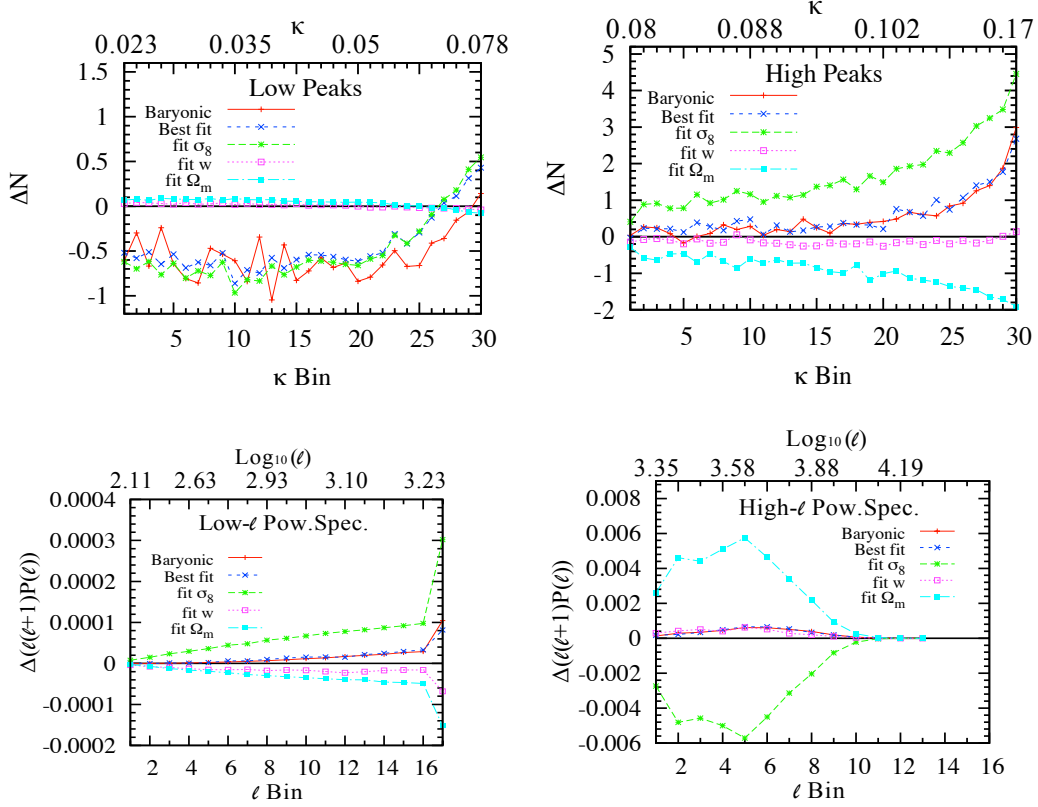


FIG. 7: The figure compares the changes in the peak counts and the power spectra caused by the presence of baryons (solid red curves), and by the biased cosmological parameters in the best-fit baryonless models (dashed blue curves). For every curve, the corresponding values in the fiducial, baryonless model is subtracted, so that only the offsets from this fiducial model are shown. The four panels (top left, top right, bottom left, bottom right) show the results for low peaks, high peaks, low- ℓ power spectrum and high- ℓ power spectrum, respectively. Bin numbers are shown on the bottom x axis, with corresponding κ and ℓ values indicated on the top of the figure (note that the binning is not linear in κ and ℓ ; see § III B of the text for a full description of the binning scheme). In general, the biased cosmologies are able to mimic the effect of baryons remarkably well. The long-dashed [green], dotted [pink] and dot-dashed [cyan] curves show the “decomposition” of the biased best-fit cosmology among the three cosmological parameters: they show the effect of changing a single one of the three parameters σ_8 , w , Ω_m at a time to its best fit value. (The green, pink and cyan curves sum up to the blue curve.)

onic models were fitted with the non-baryonic models, using linear interpolation and backward finite difference derivatives. Unless the model being evaluated is very close to one of the simulated cosmologies, there is no clear reason to prefer either the forward or the backward derivative. One concern is whether our results on the inferred biases change if we use different derivatives (or a 2nd order Taylor expansion). To investigate this, we repeated our analysis using backward and “2-sided” derivatives. In Table IV, we show the biases of the three cosmological parameters σ_8 , w , Ω_m inferred from the peak counts, with all three types of derivatives. As the table shows, the biases from the low peaks remain similar (or at least negligible, within errors) for each type of derivative. However, high peaks have large and significant differences in the biases.

These difference may indicate a genuine asymmetry in the cosmology-dependence of the peak counts, but the differences may be partly a numerical artifact due to the

σ_8 - Ω_m degeneracy. Given the cosmology-dependence of the peak counts (see, e.g., Figure 8 in ref. [24]), it is apparent that increases in σ_8 can be mostly compensated by decreases in Ω_m , and vice versa (see also ref. [19]). It is easy to imagine that as a result of this degeneracy, small changes in the baryonic peak counts that are being fit can produce large changes in the σ_8 and Ω_m biases – depending on where along the σ_8 - Ω_m degeneracy curve the baryonic effect forces the best-fit (the residuals could then also produce large changes in the w bias).

In addition to the high peaks, we find that the biases from the high- ℓ power spectrum also change by up to 30% between using backward vs. forward derivatives. We conclude that, unfortunately, we cannot determine the values of the biases of the high peaks and the high- ℓ power spectrum accurately: we need a larger number of WL maps to determine the derivatives with better precision, and the parameter space needs to be sampled more finely with simulations to map out the nonlinear

Observable	derivative	$\Delta\sigma_8$	Δw	$\Delta\Omega_m$
Low Peaks	backward	0.009	0.01	-0.001
	forward	0.012	0.00	-0.002
	2-sides	0.009	0.01	—
High Peaks	backward	0.061	0.10	-0.024
	forward	0.035	0.05	-0.009
	2-sides	0.026	0.09	—

TABLE IV: *The biases of the three cosmological parameters σ_8 , w , Ω_m inferred from the peak counts, using three different types of finite-difference derivatives. The baryonic models were again fit by non-baryonic models, using linear interpolations with either backward, forward, or “two-sided” derivatives, to make predictions for cosmologies in-between those that we simulated. (The biases for Ω_m in the high peak case for the 2-sided derivative could not be determined reliably, owing to numerical issues related to the discontinuous switch in the derivative type at the fiducial Ω_m .)*

dependence of the observables on the cosmological parameters. Nonetheless, our overall conclusion, namely that the low peaks and the low- ℓ power spectrum are unbiased, while high peaks and the high- ℓ power spectrum are noticeably biased, holds for all types of derivative we have tried. Furthermore, it would be a remarkable coincidence if the true biases from the latter two observables turned out to be in a degenerate direction; we therefore also expect our generic conclusion about the possibility of “self-calibration” to remain valid.

How robust are the results to the number of realizations of the baryonic maps? As mentioned above, our results are ultimately based on the 200 baryonic maps in the fiducial cosmology. To show that these 200 baryonic maps are sufficient to capture the systematic changes caused by the baryon cooling, in Table V, we compare the biases of the cosmological parameters inferred from 100 vs. 200 realizations of baryonic maps. We found that the biases from 200 baryonic maps are close to the biases from 100 baryonic maps, with the differences of < 0.002 in $\Delta\sigma_8$, < 0.01 in Δw and < 0.002 in $\Delta\Omega_m$. These differences are smaller than the uncertainties on the biases discussed above. This is in reassuring contrast to the apparently high demand on the accuracy of the derivatives, where not even 1000 maps are enough to get stable biases for high peaks and the high- ℓ power spectrum. It is also worth noting that when we tried to repeat our analysis using only 50 realizations, we found significant differences in the biases. This shows that the baryonic effects on the peak counts vary from one realization to another, and at least $\gtrsim 100$ realizations are required to quantify them reliably. Interestingly, we have found that the baryonic effect on the power spectrum is much more systematic, with little variation from one map to another (see discussion below).

Effect of noise. An important question is how sensitive our results are to the presence of galaxy shape noise. To address this issue, we have repeated our analysis without adding noise to the maps. Naively, one expects that noise might suppress the baryon-induced differences in

Observable	# of realizations	$\Delta\sigma_8$	Δw	$\Delta\Omega_m$
Low Peaks	100	0.011	0.010	-0.001
	200	0.009	0.005	-0.001
High Peaks	100	0.059	0.101	-0.023
	200	0.061	0.103	-0.024

TABLE V: *The biases of the three cosmological parameters σ_8 , w , Ω_m inferred from the peak counts, based on either 100 or 200 realizations of the baryonic maps.*

the peak counts. This expectation is confirmed by Figure 5, which shows, in particular, that the range of peak heights that are unaffected is much narrower in the noiseless case than in the noisy case. We therefore proceed by re-defining the low- and high-peaks in the noiseless maps to be those with heights between $0 \leq \kappa_{\text{peak}} \leq \sigma_0$ and $\kappa_{\text{peak}} \geq \sigma_0$. Here $\sigma_0 = 0.022$ denotes the standard deviation of the convergence κ in the absence of noise, and corresponds roughly to where baryon effects become significant (see the red curve in Fig. 5).

The biases of the cosmological parameters inferred from the low peaks are found to be $(\Delta\sigma_8, \Delta w, \Delta\Omega_m) = (-0.005, 0.09, 0.001)$. For high peaks the biases are $(\Delta\sigma_8, \Delta w, \Delta\Omega_m) = (0.017, 0.24, 0.006)$. These noiseless bias vectors are generally different from those in the noisy case (rows with 200 realizations in Table V). As in the noisy case, the biases from the low peaks are still much smaller than from the high peaks (we have verified that this is also true for the forward and 2-sides derivatives). However, the simple expectation that noise reduces the bias holds only for both low- and high peaks for w . The noise *increases* the bias in σ_8 for both types of peaks. Finally, the Ω_m -bias is decreased by noise for low peaks, but increased for high peaks. In our analysis, we have assumed that the noise is Gaussian, and is known perfectly. The above changes in the bias vectors imply that precise measurements of the shape noise will indeed be crucial when attempting to model baryon effects in the WL data.

We have also found that the biases in the noiseless maps are not as stable with respect to the number of realizations as in the noisy case. The worst case from backward derivative is the noiseless low peaks. For example, when we use 100 realizations, the biases change by a factor of \approx two, to $(\Delta\sigma_8, \Delta w, \Delta\Omega_m) = (-0.011, 0.05, 0.003)$. As we will see in the next paragraph, this is in contrast with the behaviour of the bias from the power spectrum, which is always very stable to number of realizations. A possible explanation of this difference is that changing the concentration parameter can impact any individual peak either way. This is because the change in the contribution κ to a peak from an individual halo can be positive or negative, depending on the impact parameter of the halo; halos contributing (especially to the low) peaks have a broad range of impact parameters (these points will be demonstrated in Figure 9 below). This effect is reduced in the presence of noise, since noise itself tends to give the largest contribution of κ to low peaks.

Robustness of biases from the power spectrum. As mentioned above, we have found that the results from the power spectrum, both with and without noise, are always very robust with respect to the number of realizations of baryonic maps. The small sizes of the error bars in Figure 4 already show that baryonic effects have much weaker map-to-map variations, compared to those in Figure 5. The differences in the biases inferred from 200 vs. 100 realizations are less than 0.001 in $\Delta\sigma_8$, 0.01 in Δw and 0.001 in $\Delta\Omega_m$. In fact, we have found that for the power spectrum at $\ell \geq 2000$, even a *single* map is sufficient to determine the biases with $\lesssim 10\%$ accuracy. For the power spectrum at $\ell \leq 2000$, which is numerically somewhat less stable than the high- ℓ power spectrum, we have found that $\gtrsim 5$ maps are needed to achieve the same accuracy. These numbers refer to the noisy maps; in the noiseless case, the $\ell \leq 2000$ power spectrum would require $\gtrsim 10$ maps.

The biases from the power spectra are more sensitive to derivative types, with absolute changes comparable to those for the peaks. However, compared to peaks, the biases from the power spectra are larger to begin with, making the biases more stable in a fractional sense. The differences in biases from the power spectra with and without noise are $< 30\%$; the only exception is the noisy case and the high- ℓ range, for which there is a change by a factor of 2 in Δw . We have studied the sensitivity to the number of bins only for the high- ℓ case (this is because we did not have a sufficient number of pre-bins saved in the low and very low- ℓ ranges to increase the resolution in those cases). In our fiducial set of computations above, we used 13 high ℓ bins. We found that as we increase the number of bins from 13 to 15 to 20, the changes in the biases are comparable to those for the high peaks, with the 13-to-15-change being a bit smaller than the 13-to-20-change. However, again because the power spectrum in general has much larger absolute biases, even in the worst case, changing from 13 to 20 bins, the corresponding fractional change in the parameter biases is low ($\lesssim 15\%$).

B. Cosmology from low-bias statistics

We have shown that baryon cooling causes a strong increase in the number of high peaks and the small scale power spectrum. The number of low-amplitude peaks and the large-scale power spectrum are both relatively insensitive to baryon cooling, and thus deliver nearly bias-free cosmological constraints. Figure 6 reveals that the area of the marginalized 2D error contours from these low-biased statistics are roughly comparable to those from their more biased counterparts. In this section, we will further explore how much of the cosmological sensitivity resides in the low-bias statistics.

To assess the fraction of the cosmological sensitivity coming from low peaks and large-scale power spectra, we first computed a $\Delta\chi^2$, analogous to the quantity defined

Observable	FOM (all)	FOM (low-bias)	Fraction (low/all)	Fraction per parameter
Peaks	$1.30 \cdot 10^6$	$0.723 \cdot 10^6$	0.56	0.82
Pow. Spec.	$1.10 \cdot 10^6$	$0.060 \cdot 10^6$	0.055	0.38

TABLE VI: *The strength of the cosmological constraints for peak counts and power spectrum, expressed in terms of a figure of merit (FOM; defined as the inverse of the three-dimensional error volume in the σ_8, Ω_m, w parameter space). FOM values are compared for the relatively unbiased low-amplitude peaks and very low- ℓ ($100 < \ell < 1000$) power spectrum (second column) vs. all peaks and the power spectrum on all scales (first column). The third column indicates the ratios of these FOM (indicating the fraction of the cosmological constraints contained in the low-bias ranges of both statistics), while the rightmost column shows the cube root of this ratio (a rough estimate of the fraction of the constraint on individual parameters).*

in Eq. (9) above, except using the difference ΔN between the mean number of peak in pairs of CDM simulations with different σ_8 , w and Ω_m . This measures the significance of the differences caused by the changes in the individual cosmological parameters. We find that the $\Delta\chi^2$ values from the relatively unbiased low-amplitude peaks exceed half of the $\Delta\chi^2$ values obtained from all peaks. On the other hand, the $\Delta\chi^2$ values from the large-scale power spectrum are typically reduced by a factor of ~ 5 compared to using the power spectrum on all scales (the exception is w , for which the large angular scales contain \approx half of the total $\Delta\chi^2$).

The above shows that the low peaks contain most of the raw cosmological sensitivity to each individual parameter, but it neglects degeneracies among parameters, which ultimately drive the marginalized constraints. We therefore next assess the fraction of the full cosmological sensitivity, coming from low peaks and large-scale power spectra, when all three parameters are simultaneously varied. For this purpose, we repeated our analysis as outlined in this paper, except we bootstrapped the CDM maps from our 45-simulation map set, rather than the baryonic maps. This yields constraint in the three-dimensional parameter space σ_8 , w and Ω_m . We measure the three-dimensional volumes in the parameter space containing 68% of the probability for all peaks and low peaks separately, and likewise for the very low- ℓ and the full power spectra. The figure of merit (FOM) is defined to be the inverse of these volumes, and indicates the overall strength of the constraints. The ratio of the FOM from low vs. all peaks and the very low- ℓ vs. the full power spectra then captures the “fraction” of the full cosmological sensitivity in the unbiased statistics. This ratio can be converted roughly into a per-parameter estimate by taking the third root, although the differences in constraints on individual parameters would of course depend on the exact shape of the constraint volume. We list these quantities in Table VI.

As is evident from the table, the peaks and the power spectrum deliver comparable FOMs when the whole

range is used. However, the essentially unbiased low-amplitude peaks contain more than half (a fraction 0.56) of the FOM, whereas this fraction is only ~ 0.05 for the very low- ℓ power spectrum (the latter increasing to ~ 0.16 if multipoles up to $\ell < 2000$ are included). In terms of the fraction per parameter, the low peaks contain approximately 82% of the information, whereas the very low- ℓ power spectrum contains 38% (the latter number increasing to 54% with multipoles up to $\ell < 2000$). We conclude that the low-bias statistics contain the (slight) majority of the cosmological sensitivity for peaks, but a relatively small fraction for the power spectrum.

C. The insensitivity of low peaks to baryon cooling

We next examine why the number of low peaks is insensitive to baryon cooling, as modeled by an increase in the halo concentration parameters. In short, we attribute the lack of sensitivity to two reasons: halos contributing to low peaks have large off-sets from the line-of-sight toward each peak (and therefore the light rays do not “see” the halo cores) and also relatively low masses (so that the details of the projected halo density profiles are “washed out” by the 1-arcmin smoothing). We demonstrate these points explicitly below.

In Figure 8, we show the distribution of the impact parameters (in units of R_{180}) at which light rays, corresponding to the centers of WL peaks, intersect dark matter halos along the line of sight. Following ref. [24], for each peak, we identify all halos along the sightline, and rank them by their contribution to the peak’s height. Going down this ranked list (beginning with halos with the largest contribution), we sum the κ contributions from the first n halos until these n halos account for $\geq 50\%$ of the total halo contribution to the peak convergence. This procedure assigns the number n to each peak (hereafter referred to as an “ n -halo peak”).

The top panel relates to high peaks (with heights of $\kappa \geq 0.08$), which are typically produced by one or two halos. The panel shows, separately, the impact-parameter distribution for the dominant halos for 1-halo peaks, and for 2-halo peaks. Low peaks (with heights between $\sigma_{\text{noise}} \leq \kappa_{\text{peak}} \leq 0.08$; with $\sigma_{\text{noise}} = 0.023$) are typically produced by 4-8 halos. The representative case of 5-halo peaks is shown in the bottom panel. Our baryonic model, with a 50% boost in the concentration parameter, was used for this figure (with source galaxies at redshift $z_s = 2$ and with galaxy shape noise and 1 arcmin smoothing included as before).

As the figure shows, for high peaks, the light rays typically go near the halo centers, with impact parameters $< 0.2R_{180}$. In contrast, for low peaks, the light rays have large impact parameters, with a maximum near $\approx 0.6R_{180}$. This is as expected: as more halos contribute to a peak, the contribution from each halo is lower, and the halos are less precisely aligned along the line of sight.

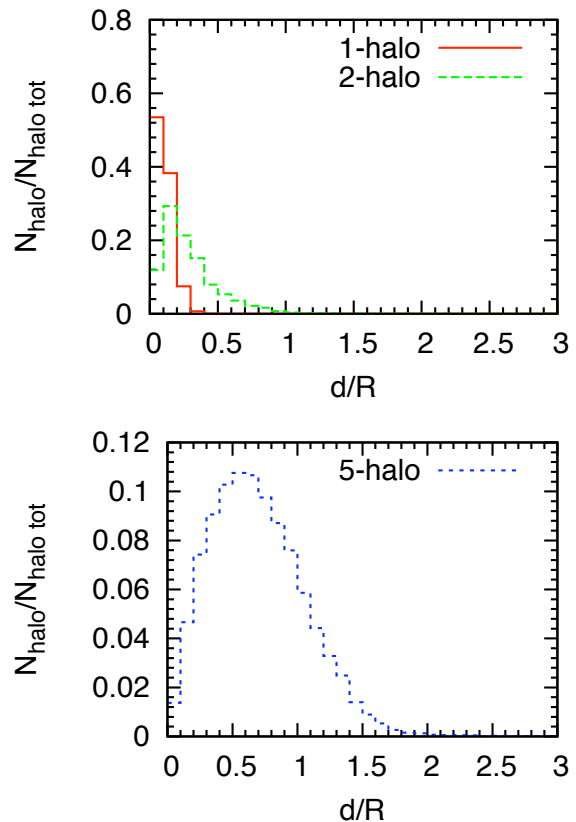


FIG. 8: The distribution of the impact parameters (in units of the virial radius) at which light rays, corresponding to the centers of WL peaks, intersect dark matter halos along the line of sight. The upper panel is for high peaks, which are typically produced by one or two halos. The panel shows, separately, the impact-parameter distribution for the dominant halos for 1-halo peaks (solid red curve), and for 2-halo peaks (dashed green curve). “ n -halo peaks” are defined to be those for which the sum of n halos along the line of sight accounts for at least 50% of the halo contribution to the total peak convergence. The light rays typically go near the halo centers, with impact parameters $< 0.2R_{180}$. In contrast, for the low peaks, shown in the lower panel, the light rays have a large impact parameter. These peaks are typically produced by 4-8 halos; the panel shows the distribution for the typical case of 5-halo peaks, which has a maximum at $\approx 0.6R_{180}$.

Figure 9 shows the fractional difference in the convergence contribution from halos, caused by a 50% increase in their concentration, as a function of the impact parameter (in units of the halo’s virial radius R_{180}). The three curves correspond to halos with masses of 10^{12} , 10^{13} , and $10^{14}h^{-1}M_{\odot}$, as labeled. The halos and source galaxies are located at redshift $z = 0.5$ and $z_s = 2$, respectively and we assume the halos have NFW profiles, with a concentration parameter (before the 50% boost) given by Eq. (4). As the figure shows, lower-mass halos are less affected by the boost in concentration. These halos are more compact, and the 1 arcmin smoothing makes their

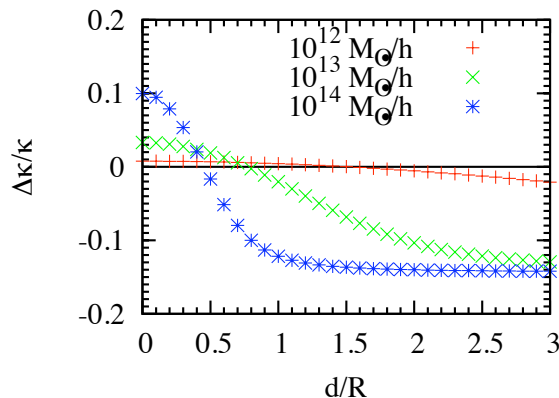


FIG. 9: The figure shows the fractional difference in the convergence contribution from halos, caused by a 50% increase in their concentration, as a function of the impact parameter d (in units of the halo’s virial radius R_{180}). The red plus signs, green crosses, and blue snowflakes correspond to halos with masses of 10^{12} , 10^{13} , and $10^{14} h^{-1} M_{\odot}$, as labeled. The halos and source galaxies are located at redshift $z = 0.5$ and $z_s = 2$, respectively and we assume the halos have NFW profiles, with a concentration parameter (before the 50% boost) given by Eq. (4). Lower-mass halos are less affected by the boost in concentration. These halos are more compact, and the 1 arcmin smoothing makes their convergence contribution less sensitive to their intrinsic density profile.

convergence contribution less sensitive to their intrinsic density profile.

Figures 8 and 9 together allows us to assess the sensitivity of peak counts to baryons for both high and low peaks. High peaks are dominated by halos with higher masses $10^{13} - 10^{14} h^{-1} M_{\odot}$, and the dominant halos for the 1-halo peaks have masses near the upper end of this mass range. On the other hand, the low peaks are dominated by halos with lower masses, between $10^{12} - 10^{13} h^{-1} M_{\odot}$. Combining the results from Figures 8 and 9, we see that high peaks with masses $\lesssim 10^{14} h^{-1} M_{\odot}$ and impact parameters $< 0.2 R_{180}$ have typical fractional differences of about 8 percent. By comparison, low peaks with masses $10^{12} - 10^{13} h^{-1} M_{\odot}$ and impact parameters $\approx 0.6 R_{180}$, have typical fractional differences of about 2 percent, much lower than high peaks. This explains why the low peaks are less sensitive to baryon cooling.

V. SUMMARY AND CONCLUSIONS

In this paper, we have studied the impact of the cooling and concentration of baryons in dark matter halos on WL observables, by manually steepening the density profile of each DM halo in a suite of ray-tracing N-body simulations. Our main findings are that a) the low peaks ($0.023 \leq \kappa_{peak} \leq 0.08$) are mostly unaffected, b) high peaks ($\kappa_{peak} \geq 0.08$) and the power spectrum at $\ell > 1,000$ lead to biases if baryonic effects are ne-

glected in the cosmological parameter estimation, c) the bias in high peaks is comparable to the bias for the low- ℓ ($\ell < 2000$) power spectrum, and d) the high- ℓ ($2000 < \ell < 20,000$) power spectrum exhibits a much stronger bias in a different direction.

We find a large increase in the amplitude of the small-scale power spectrum, caused by the steepening of halo profiles, confirming previous works. It is unsurprising that we find a corresponding large increase in the number of high peaks, since these peaks are typically caused by individual halos. However, the fact that low peaks are essentially insensitive to an increase in the halo concentration was surprising (at least to us). This is an especially important finding, since these low peaks contain the majority of the cosmological information contained in the entire set of peaks. We attribute the robustness of these low peak to the fact that they are created by an alignment of typically 4–8 of low-mass ($\sim 10^{12} - 10^{13} M_{\odot}$) halos [24], with each halo typically offset from the line-of-sight towards the peak by a fair fraction of the virial radius ($\sim 0.5 R_{vir}$). As a result, light-rays corresponding to the peak do not pierce the cores of these halos, where baryonic effects are most significant. Additionally, the halos contributing to the low peaks are compact on the sky. As a result, when their intrinsic profiles are convolved with the smoothing filter (with an angular scale of 1 arcmin in our case), applied to the raw convergence maps, the details of the profiles are washed out.

We have explicitly computed the biases in the cosmological parameters w , σ_8 and Ω_m when peak counts and power spectra are fit neglecting the baryonic effects. We find that the biases from the low peaks and from the very low- ℓ power spectrum ($\ell < 1000$) are small (consistent with zero within errors). The biases from high peaks and from the low- ℓ power spectrum ($\ell < 2000$) are significant and comparable both in magnitude and sign (e.g. both biases are $\Delta w \approx +0.1$ for dark energy). It is an important result that the high peaks are no more biased than the low- ℓ power spectrum ($\ell < 2000$), the latter being the range of scales in the baseline plans by the LSST WL survey, to infer cosmological parameters [49].

Our finding that biases from the high- ℓ power spectrum ($2000 < \ell < 2 \times 10^4$) are very large (between $\Delta w = -0.3$ and -0.6), but in a very different direction in the (w, σ_8, Ω_m) parameter space than the bias from high peaks, also has an important general implication. It suggests the possibility of an effective self-calibration, by tuning the concentration parameter to bring the different contours in the cosmological parameter space into alignment. However, given the large magnitude of this bias, and keeping in mind that additional unknown “baryonic parameters” will be present in a fully realistic case, it is difficult to see how this self-calibration could be achieved to the sub-percent accuracy level targeted by LSST. We note, however, that biases from the power spectrum extended down to $\ell < 2,000$ are lower, and still in a modestly different direction than that of the high peaks, possibly allowing more accurate self-calibration. Until bary-

onic effects are much better understood, it may be advantageous to restrict the analysis to statistics that are nearly unbiased, such as the low peaks and the very low ($\ell < 1,000$) power spectrum we identify here. Our result suggests that in the case of peaks, less than half of the cosmological constraining power may be lost.

Our two main qualitative results are likely robust: constraints from sufficiently low-amplitude peaks will be relatively unbiased; and some form of self-calibration will likely be realized in a real survey. However, our study is clearly highly idealized. We have identified a number of caveats arising from our toy model for the impact of astrophysical processes, our limited number of simulations (both in terms of sampling the cosmological parameter space and in terms of the number of realizations), our simplified treatment of source galaxies, noise, and our neglect of all instrumental errors. Our results call for follow-up work with more extensive simulations and more realistic modeling, to address these shortcomings.

Acknowledgments

This research utilized resources at the New York Center for Computational Sciences, a cooperative effort between Brookhaven National Laboratory and Stony Brook University, supported in part by the State of New York. This work is supported in part by the U.S. Department of Energy under Contract No. DE-AC02-98CH10886 and by the NSF under grant AST-1210877. JMK and KMH acknowledge support from NASA’s Jet Propulsion Laboratory through Contract 1363745. The simulations and non-baryonic WL maps were created on the IBM Blue Gene/L and /P New York Blue. The baryonic maps were created and the analyses were performed on the LSST/Astro Linux cluster at BNL.

-
- [1] A. Albrecht *et al.*, arXiv:astro-ph/0609591.
 - [2] H. Hoekstra and B. Jain, Annual Review of Nuclear and Particle Science **58**, 99 (2008), [arXiv:0805.0139].
 - [3] D. Munshi, P. Valageas, L. van Waerbeke and A. Heavens, Phys. Rep. **462**, 67 (2008), [arXiv:astro-ph/0612667].
 - [4] J. A. Tyson, R. A. Wenk and F. Valdes, ApJL **349**, L1 (1990).
 - [5] T. Schrabback *et al.*, A&A **516**, A63 (2010), [arXiv:0911.0053].
 - [6] E. Semboloni, T. Schrabback, L. van Waerbeke, S. Vafaei, J. Hartlap and S. Hilbert, MNRAS **410**, 143 (2011), [arXiv:1005.4941].
 - [7] Forthcoming and planned surveys include those by LSST (www.lsst.org), by Hyper Suprime-Cam (HSC, www.naoj.org/Projects/HSC/HSCProject.html), the Dark Energy Survey (DES, www.darkenergysurvey.org), the Kilo-Degree Survey (KIDS, <http://kids.strw.leidenuniv.nl>), Pan-STARRS (<http://pan-starrs.ifa.hawaii.edu/public>), and Euclid (<http://sci.esa.int/euclid>).
 - [8] B. Jain and L. Van Waerbeke, ApJL **530**, L1 (2000), [arXiv:astro-ph/9910459].
 - [9] B. Jain, U. Seljak and S. White, ApJ **530**, 547 (2000), [arXiv:astro-ph/9901191].
 - [10] S. Wang, Z. Haiman and M. May, ApJ **691**, 547 (2009), [arXiv:0809.4052].
 - [11] J. Sato, M. Takada, Y. P. Jing and T. Futamase, ApJL **551**, L5 (2001), [arXiv:astro-ph/0104015].
 - [12] A. C. C. Guimaraes, MNRAS **337**, 631 (2002), [arXiv:astro-ph/0202507].
 - [13] M. Maturi, C. Angrick, F. Pace and M. Bartelmann, A&A **519**, A23 (2010), [arXiv:0907.1849].
 - [14] D. Munshi, L. van Waerbeke, J. Smidt and P. Coles, MNRAS **419**, 536 (2012), [arXiv:1103.1876].
 - [15] J. M. Kratochvil, E. A. Lim, S. Wang, Z. Haiman, M. May and K. Hufenberger, Phys. Rev. D **85**, 103513 (2012), [arXiv:1109.6334].
 - [16] S. Pires, J.-L. Starck, A. Amara, A. Réfrégier and R. Teyssier, A&A **505**, 969 (2009).
 - [17] L. Marian, R. E. Smith and G. M. Bernstein, ApJL **698**, L33 (2009), [arXiv:0811.1991].
 - [18] L. Marian, R. E. Smith and G. M. Bernstein, ApJ **709**, 286 (2010), [arXiv:0912.0261].
 - [19] J. P. Dietrich and J. Hartlap, MNRAS **402**, 1049 (2010), [arXiv:0906.3512].
 - [20] J. M. Kratochvil, Z. Haiman and M. May, Phys. Rev. D **81**, 043519 (2010).
 - [21] M. Li, ChA&A **35**, 349 (2011).
 - [22] L. Marian, S. Hilbert, R. E. Smith, P. Schneider and V. Desjacques, ApJL **728**, L13 (2011), [arXiv:1010.5242].
 - [23] M. Maturi, C. Fedeli and L. Moscardini, MNRAS **416**, 2527 (2011), [arXiv:1101.4175].
 - [24] X. Yang, J. M. Kratochvil, S. Wang, E. A. Lim, Z. Haiman and M. May, Phys. Rev. D **84**, 043529 (2011), [arXiv:1109.6333].
 - [25] L. Marian, R. E. Smith, S. Hilbert and P. Schneider, MNRAS **423**, 1711 (2012), [arXiv:1110.4635].
 - [26] S. Pires, A. Leonard and J.-L. Starck, MNRAS **423**, 983 (2012), [arXiv:1203.2877].
 - [27] J. T. VanderPlas, A. J. Connolly, B. Jain and M. Jarvis, ApJ **744**, 180 (2012), [arXiv:1109.5175].
 - [28] D. Huterer and M. White, Phys. Rev. D **72**, 043002 (2005), [arXiv:astro-ph/0501451].
 - [29] H. Zhan and L. Knox, ApJL **616**, L75 (2004), [arXiv:astro-ph/0409198].
 - [30] A. R. Zentner, D. H. Rudd and W. Hu, Phys. Rev. D **77**, 043507 (2008), [arXiv:0709.4029].
 - [31] M. P. van Daalen, J. Schaye, C. M. Booth and C. Dalla Vecchia, MNRAS **415**, 3649 (2011), [arXiv:1104.1174].
 - [32] E. Semboloni, H. Hoekstra, J. Schaye, M. P. van Daalen and I. G. McCarthy, MNRAS **417**, 2020 (2011), [arXiv:1105.1075].
 - [33] D. H. Rudd, A. R. Zentner and A. V. Kravtsov, ApJ **672**, 19 (2008), [arXiv:astro-ph/0703741].
 - [34] J. F. Navarro, C. S. Frenk and S. D. M. White, ApJ **490**, 493 (1997).
 - [35] J. M. Kratochvil, “The INSPECTOR GADGET Weak Lens-

- ing Simulation Pipeline: I. The Codes” (unpublished) .
- [36] J. M. Kratochvil, M. May, Z. Haiman, K. Huffenberger, D. Bard, B. Calabro and X. Yang, “The INSPECTOR GADGET Weak Lensing Simulation Pipeline: II. The First Dataset” (unpublished) .
 - [37] A. Lewis, A. Challinor and A. Lasenby, *ApJ* **538**, 473 (2000), [arXiv:astro-ph/9911177].
 - [38] V. Springel, *MNRAS* **364**, 1105 (2005), [arXiv:astro-ph/0505010].
 - [39] T. Hamana and Y. Mellier, *MNRAS* **327**, 169 (2001), [arXiv:astro-ph/0101333].
 - [40] P. Schneider, J. Ehlers and E. E. Falco, *Gravitational Lenses* (Springer-Verlag, New York, 1992).
 - [41] J. Wambsganss, R. Cen and J. P. Ostriker, *ApJ* **494**, 29 (1998).
 - [42] B. Jain, U. Seljak and S. White, *ApJ* **530**, 547 (2000), [arXiv:astro-ph/9901191].
 - [43] R. W. Hockney and J. W. Eastwood, *Computer simulation using particles* (Adam Hilger, Bristol, 1988).
 - [44] S. R. Knollmann and A. Knebe, *ApJS* **182**, 608 (2009).
 - [45] D. Nagai and A. V. Kravtsov, *ApJ* **618**, 557 (2005), [arXiv:astro-ph/0408273].
 - [46] A. F. Neto, L. Gao, P. Bett, S. Cole, J. F. Navarro, C. S. Frenk, S. D. M. White, V. Springel and A. Jenkins, *MNRAS* **381**, 1450 (2007), [arXiv:0706.2919].
 - [47] R. E. Smith, J. A. Peacock, A. Jenkins, S. D. M. White, C. S. Frenk, F. R. Pearce, P. A. Thomas, G. Efstathiou and H. M. P. Couchman, *MNRAS* **341**, 1311 (2003), [arXiv:astro-ph/0207664].
 - [48] J. R. Bond and G. Efstathiou, *MNRAS* **226**, 655 (1987).
 - [49] LSST Science Collaborations *et al.*, *ArXiv e-prints* (2009), [arXiv:0912.0201].